Unsteady Flow Interactions Within the Inlet Cavity of a Turbine Rotor Tip Labyrinth Seal

A. Pfau
e-mail: a.pfau@freesurf.ch

J. Schlienger

D. Rusch

A. I. Kalfas

R. S. Abhari

Turbomachinery Laboratory,
Swiss Federal Institute of Technology,
8092 Zurich, Switzerland

This paper focuses on the flow within the inlet cavity of a turbine rotor tip labyrinth seal of a two stage axial research turbine. Highly resolved, steady and unsteady three-dimensional flow data are presented. The probes used here are a miniature five-hole probe of 0.9 mm head diameter and the novel virtual four sensor fast response aerodynamic probe (FRAP) with a head diameter of 0.84 mm. *The cavity flow itself is not only a loss producing area due to mixing and vortex stretching, it also adversely affects the following rotor passage through the fluid that is spilled into the main flow. The associated fluctuating mass flow has a relatively low total pressure and results in a negative incidence to the rotor tip blade profile section. The dominating kinematic flow feature in the region between cavity and main flow is a toroidal vortex, which is swirling at high circumferential velocity. It is fed by strong shear and end wall fluid from the pressure side of the stator passage. The static pressure field interaction between the moving rotor leading edges and the stator trailing edges is one driving force of the cavity flow. It forces the toroidal vortex to be stretched in space and time. A comprehensive flow model including the drivers of this toroidal vortex is proposed. This labyrinth seal configuration results in about 1.6% turbine efficiency reduction. This is the first in a series of papers focusing on turbine loss mechanisms in shrouded axial turbines. Additional measurements have been made with variations in seal clearance gap. Initial indications show that variation in the gap has a major effect on flow structures and turbine loss.*
[DOI: 10.1115/1.2008973]

Introduction

The development of turbo machinery blade design is currently focusing on the characteristics of highly loaded stages. These are advantageous because the use of fewer blades that produce the same power at the same efficiency results in a substantially lower cost and a higher power density. Concerning low aspect ratio blades, as they are used in intermediate and high pressure turbines, the inherent strong secondary flows are enhanced by the design of higher turning airfoils. Consequently, the aerodynamic secondary flow losses increase.

In order to decrease secondary flows and reduce the migration of the low kinetic energy fluid into the main flow, the design of end wall regions has been increasingly addressed. Gregory-Smith et al. [1] successfully introduced the use of end wall profiling procedures to modify the secondary flow. Sauer et al. [2] proposed the use of leading edge modifications at the tip region to decrease secondary losses. These studies have shown effectiveness in controlling the secondary flow under controlled inflow conditions.

In shrouded turbines however, the inlet flow condition to a blade row is disturbed at the end wall by flow interactions with open cavities. Those open cavities are present at the inlet and exit of the labyrinth seals. The size of these cavities is determined by the axial thrust variation or the mechanical and thermal growth of the rotor assembly. As such the aerodynamic design has to allow for large inlet and exit cavities, particularly for steam turbine applications. Prior observations seem to suggest that secondary flow structures and losses are influenced by the steady and unsteady interactions with the cavity flow field.

The subject of cavity interactions in turbines was addressed the first time by Denton and Johnson [3]. However, it is only in recent years that this subject has been the focus of much research. Peters et al. [4] examined the effect of gap size on the steady interaction between the leakage flow and the secondary flow field of a subsequent stator in a 1.5 stage, shrouded axial turbine. Hunter and Manwaring [5] reported about two extra vortices generated in a downstream stator blade row. Wallis et al. [6] observed that strong interactions are present in open cavities of shrouded turbine blades. The following blade rows were found to receive the tip flow at a negative incidence. Anker and Mayer [7] numerically investigated the leakage interaction with the main flow and found that the tip leakage flow is not uniform in the pitch wise direction. Schlienger et al. [8] changed the geometry of the labyrinth exit cavities and compared the effects on the main flow as well as on the efficiency. These studies have focused mainly on the interaction happening in the main flow and following blade passages.

However, as the origins of these interactions are open cavities, an increased emphasis must be placed on the associated unsteady flow interactions within these cavities. The unsteady fluctuations may create large amplitude deviations to the time-averaged structure of the cavity flow. Thus, the actual cavity flow may be quite different than the steady model as proposed by Pfau et al. [9].

In the present work the inlet cavity to the second rotor tip labyrinth seal of a two stage axial turbine is investigated. This flow may be expected to have features similar to the unsteady wake flow avenues described by Binder [10] and unsteady vortex interactions observed by Chaluvadi et al. [11]. As the cavity region is small these flow features can only be experimentally measured with miniature probes of minimized blockage. Thus, a unique element of this work is the application of the new fast response aerodynamic probe (FRAP), which is described in a companion paper by Pfau et al. [12]. This probe provides spatially and temporally highly resolved measurements of the three-dimensional flow field.

Contributed by the International Gas Turbine Institute and presented at the International Gas Turbine and Aeroengine Congress and Exhibition, Atlanta, GA, June 16–19, 2003. Manuscript received by the IGTI December 1, 2002; final revision March 1, 2003. Paper No. 2003-GT-38271. Review Chair: H. R. Simmons.

Table 1 Main characteristics of the test turbine

Pressure ratio	1.32	Mass flow	9.86 kg/s
Max. power	400 kW	Turbine speed	2700 rpm
T_{inlet}	40 °C	P_{exit}	Ambient
Mach	0.1…0.4	Re_{Cax}	10^5
n (rotor/stator)	42	Tip diameter	800 mm
Seal gap	0.35 mm	Blade aspect ratio	1.8

Methodology

Test Case and Measurement Technology. The cavity interaction flow was investigated in the two-stage low speed axial turbine "LISA." The test rig is described in detail in Sell et al. [13] The main characteristics of the turbine are summarized in Table 1.

The constant annulus and the four blade rows are depicted in Fig. 1. The stepped shrouds on the blades together with three sealing fins form the labyrinth seal. The geometry under investigation is similar to steam turbine applications, where large inlet and exit cavities allow for axial movement of the rotor blades. Consequently, the blade profiles are of a medium loaded type with leaned stator blades.

The tip gap was set to 0.36% of the blade height. In comparison to real applications this value is small, as gaps of 0.7%–1% blade height are commonly employed. The small gap was, however, chosen in order to increase the pure cavity to main flow interaction by sucking less leakage mass flow out of the inlet cavity. The experiments were performed at a rotational speed of 2700 rpm and a mass flow of 9.86 kg/s. In real steam turbine the fluid dynamic conditions are $Re=3*10^6$ and $M=0.3$ with a suction peak velocity of around $M=0.8$. Therefore, compressibility as well as viscous effects are not exactly modeled in this turbine. However, as the velocity triangles and reduced frequencies match to a real stage, unsteady effects, like vortex or potential field interactions, are comparable.

The coordinate system used to display the results is cylindrical. The radial direction r is made dimensionless with the blade height, such that $R=0$ denotes the hub and $R=1$ the tip radius of the blades. The cavity floor of the labyrinth is at $R=1.22$. The direction of the turbine axis is denoted with z, where a local nondimensional coordinate Z is introduced (see also Fig. 2). It starts at the cavity entry lip and is made dimensionless with the axial width of the cavity ($z_{cav}=15$ mm). The circumferential direction is counted positive with the sense of rotation. The chosen view in the diagrams is upstream as the observer in Fig. 1 indicates. Therefore, the circumferential axis in the diagrams is reversed pointing into anti-rotational direction.

The data sets presented here comprise 2640 steady and 1725 time resolved measurement points. The 2640 steady data points are distributed onto six axial measurement planes as indicated in Fig. 2(*a*). Each plane is resolved by 23×19 points covering 1.1

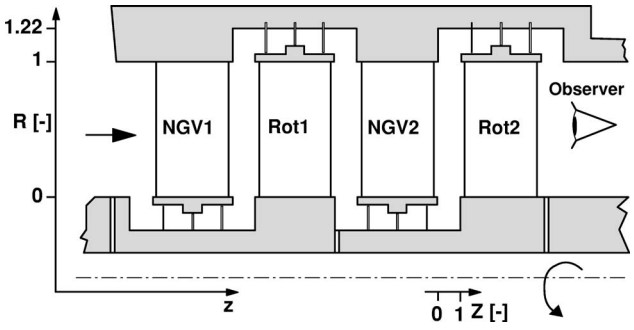

Fig. 1 Cross section of the test geometry

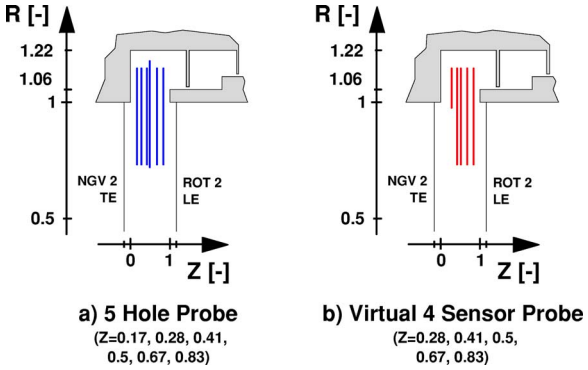

Fig. 2 Locations of measurement

pitches. A miniature five hole pneumatic probe of 0.9 mm head diameter was applied. The calibration range of the aerodynamic model was ±10° in yaw and ±30° in pitch direction. The error band width in flow angle is ±0.3° and ±60 Pa and ±120 Pa total and static pressure, respectively [14]. In terms of non-dimensional pressures C_p this equals ±0.0019 and ±0.0038 for total and static pressure. Downstream of a stator, flow velocities of $M=0.3$ are present, which is measured accurate to within ±1.3%. The accuracy of the velocity components depend on the flow angles. The worst case of error band width of the non-dimensional velocities was found to be ±0.007 in axial (v_z), ±0.016 in tangential (v_Θ) and ±0.005 in radial (v_r) direction.

The unsteady data points cover the same downstream five axial positions as the pneumatic data grid but with an average resolution of 23×15 points per plane [see Fig. 2(*b*)]. Due to geometric constraints the measurement plane at $Z=0.28$ ranges from the cavity floor to $R=0.95$ only. The virtual four sensor fast response aerodynamic probe, that was used, is characterized by low blockage with a head diameter of 0.84 mm and the capability of measuring three-dimensional flow up to a frequency of 25 kHz. The probe's calibration limits the range to ±30° for yaw and −30° to +21° for the pitch angle. The probe concept is described in detail in Pfau et al. [12]. Flow angles are measured to ±0.4° for yaw and ±0.8° for pitch angle. The accuracies of total and static pressure are ±120 Pa and ±85 Pa which result in a typical error of 1.2% for Mach number. These numbers do not include unsteady aerodynamic effects on the probe tip.

Unsteady Data Postprocessing. Each position of the measurement grid is measured for 3 s at 200 kHz. The data sets are processed to yield the basic flow quantities, i.e., flow angles, total and static pressure by applying a phase lock average of 100 events. One event covers three consecutive rotor blade passages. Each rotor passage is resolved by 106 samples. In comparison to the highest frequency measured in the spectrum this temporal resolution results in an over sampled data set. However, for applying fast response measurement technology in a virtual three or four sensor mode this is a necessity, so that the measured relative position to the rotor of each probe is accurately known. A detailed description of the data postprocessing is given in Pfau et al.[12]

The basic flow quantities are reduced to Mach number and velocity components. The instantaneous velocity field is further processed to calculate the instantaneous vorticity. This is possible, because the data are highly resolved in both space and time and thus, a quasi-steady analysis at each instant of time can be correctly performed. Partial time derivatives of the vorticity are calculated by applying a time marching differential scheme on the control volume data sets. Therefore, all terms of the unsteady vorticity equation can be calculated, which allows for further description of the loss production mechanisms.

The data are measured in the absolute coordinate system. The transformation into the rotating coordinate system is done by

shifting the location of data points in the rotational direction. At each time step the rotor moves 0.08°. The rotational speed is subtracted from the circumferential velocity component. Then the relative norm of the velocity as well as the relative flow angles are calculated. Adding the relative dynamic head to the static pressure field results in the relative total pressure. Time averaging within the relative frame allows the separate rotor influences on the flow field to be evaluated.

Experimental Results

Absolute Frame of Reference.

Pitch Wise Averaged Data. Measurements taken with the pneumatic five hole probe are assumed to be time averaged data and show the flow structure in the absolute frame of reference. Figure 3 presents the pitch wise averaged data at the first, middle, and last axial positions given in Fig. 2. The error band is given for each quantity.

The non-dimensional total pressure in Fig. 3(*a*) shows a strong radial gradient between $R=0.93$ and 0.99. It decays with increasing Z. At $Z=0.17$, a total pressure wake at $R=1$ and a jet at $R=0.97$ are present. The wake jet character gets mixed out at the next axial position. The cavity flow shows a lower total pressure than the main flow. Close to the rotor inlet at $Z=0.83$ the total pressure profile has a more uniform distribution at radii lower than 0.93. Note the kink in the profile at $R=1.08$ and the associated higher level of total pressure at around $R=1.03$. The effect stems from the rotating shroud leading edge entraining kinetic energy into the fluid via shear.

The static pressure distribution in Fig. 3(*b*) is showing a radial pressure gradient. It is in radial equilibrium with the centrifugal forces to keep the fluid in a swirling motion. Coming from lower span the gradient increases in the vicinity of $R=1$. Here the first and last axial positions $Z=0.17$ and 0.83 show a local maximum in contrast to the midcavity position. All axial positions encounter a local minimum of static pressure around $R=1.06$. A strong radial pressure gradient connects the local minimum to the cavity floor wall. Note that the wall pressures of $Z=0.5$ and 0.83 at $R=1.22$ are results of pitch wise averaged wall pressure tap measurements.

The axial velocity component made nondimensional with the blade tip speed is given in Fig. 3(*c*). The over and under turning effect of the flow due to the stator passage vortex is seen in the velocity profile. The local maximum at $R=0.8$ is caused by under turning and coincides with the radial position of the loss core, see also Fig. 4(*a*). The over turning leads to a kink in the axial velocity profile at $R=0.93$. Zero through flow is found around $R=1.06$. The back flow component within the cavity reaches values up to 10% of the blade tip speed. The position of the local minima shift radially downwards with increasing Z.

The radial velocity in Fig. 3(*d*) indicates a vortical flow within the cavity having negative components at $Z=0.17$ and positive components at $Z=0.83$. Note, that the absolute value at $Z=0.83$ is about 0.07 higher than at $Z=0.17$. The sense of rotation is counterclockwise resulting in positive vorticity, see also Fig. 6. The center of the vortex is characterized by a local minimum in static pressure. The local minimum in Fig. 3(*b*) at $R=1.06$ is an indication of the vortex core. This is a first evidence of a toroidal vortex within the cavity. In Fig. 3(*e*) the over and under turning behavior results in a local maximum and minimum of tangential velocity at $R=0.8$ and $R=0.93$, respectively. At $Z=0.17$ a shear layer with a strong gradient in tangential velocity connects the over turning region to a wake of low tangential momentum. It has a velocity deficit of 0.08 compared to the swirling velocity of the cavity flow and 0.2 compared to the region of over turning at $R=0.93$. Moving downstream to $Z=0.5$ the wake is filled up as tangential momentum is transferred from the main flow and the cavity flow into the wake. Close to the shroud leading edge at $Z=0.83$ the wake is filled up and has gained additional momentum. There are two

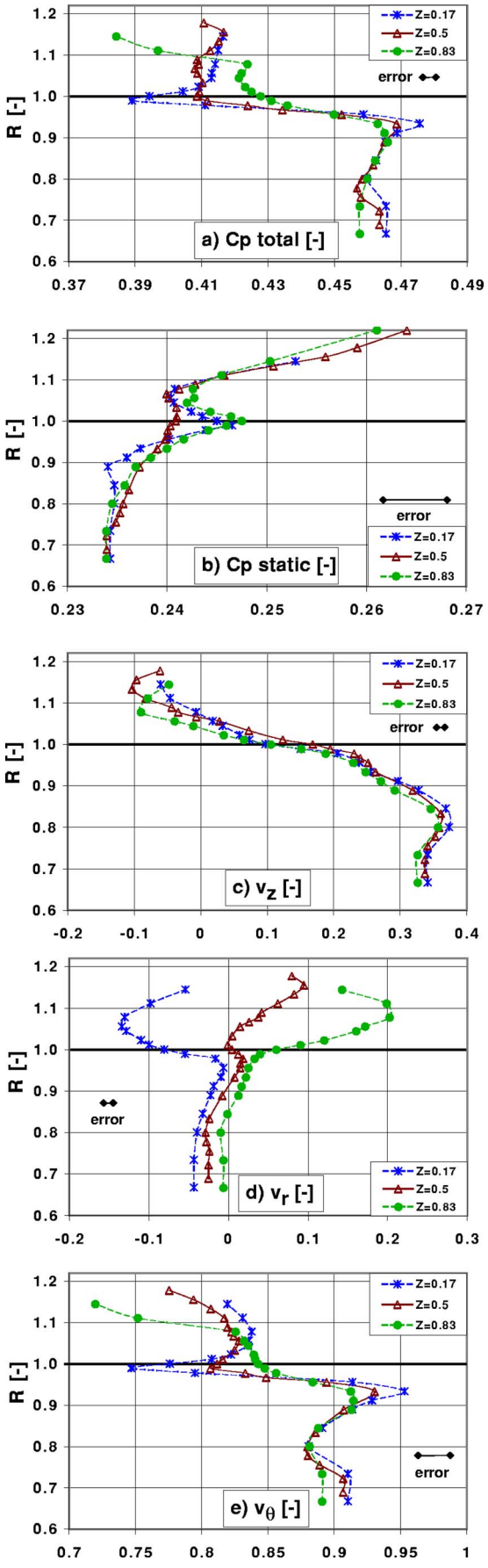

Fig. 3 Pitch wise averaged results

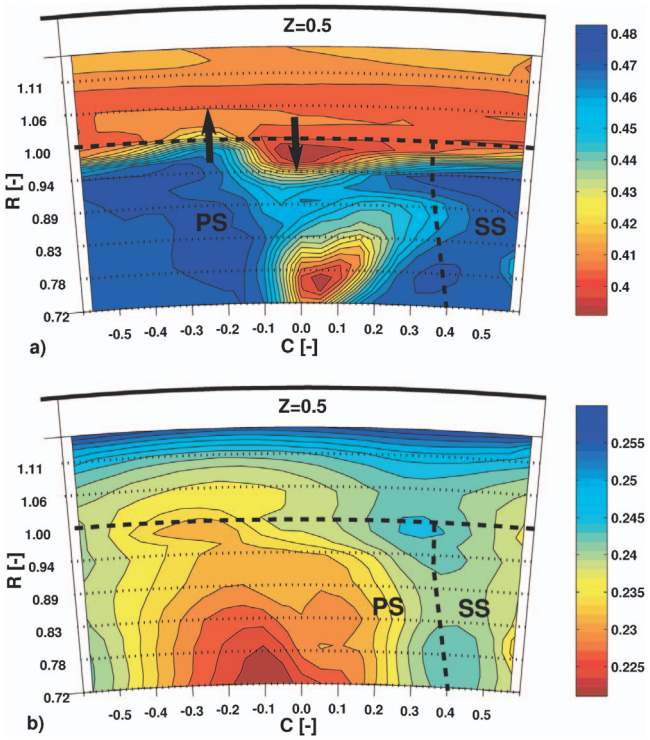

Fig. 4 ***a*) Total pressure C_{po}[−], *b*) Static pressure C_p[−]**

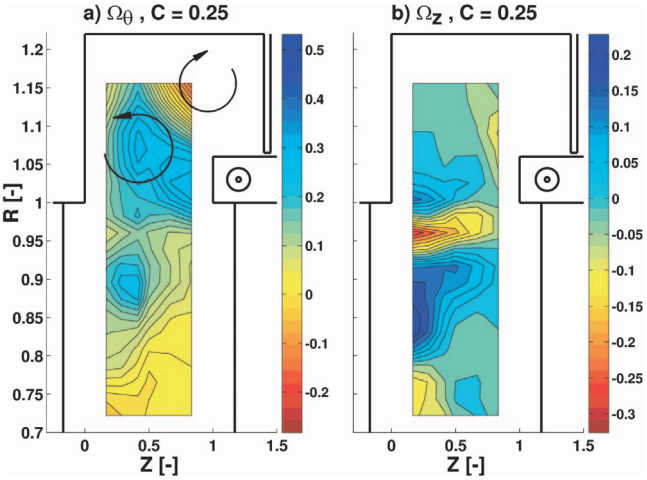

Fig. 6 Vorticity components at C=0.25

sources of tangential momentum entrainment in this flow region: the rotating shroud and the higher swirl component of the main flow. The shroud outer diameter at R=1.06 coincides with the kink in the tangential velocity profile.

Pressure and Velocity Field. The total pressure distribution at mid-cavity position Z=0.5 is displayed in Fig. 4(*a*). The cavity floor is depicted with a thick line. The tip radius and the trailing edge position of the stator are indicated with dashed lines. The distribution shows similar features as described in Pfau et al. [9]. The cavity flow has a lower level of total pressure. The main flow exhibits the secondary flow structure of a blade passage showing a loss core at R=0.76. On the pressure side of the stator wake the high total pressure gradient reaches the tip radius R=1. Here the thin boundary layer created on the passage tip end wall meets the cavity flow. The fluid has positive radial velocity and is moving into the cavity as the arrow indicates. Above the loss core, i.e., on the suction side of the blade wake, a low total pressure region has formed at R=0.97 showing the same order of magnitude as the loss core. This region is part of a wake in tangential momentum, as described in Fig. 3(*e*). It originates from the backward facing surface of the cavity at a radial position slightly higher than 1. The arrow illustrates the negative radial velocity and the flow out of the cavity.

The static pressure field in Fig. 4(*b*) is circumferential nonuniform due to the stator trailing edge. Close to the position of the trailing edge around C=0.35 a high static pressure is induced. At C=−0.1 the distance to the suction side surface is larger and therefore the static pressure is lower. This circumferential distribution propagates into the cavity volume and varies over one pitch by ±0.003 at R=1.06.

Comparing Figs. 4(*a*) and 4(*b*) the blade wake has convected ΔC=−0.4 from the trailing edge position. The local minimum in

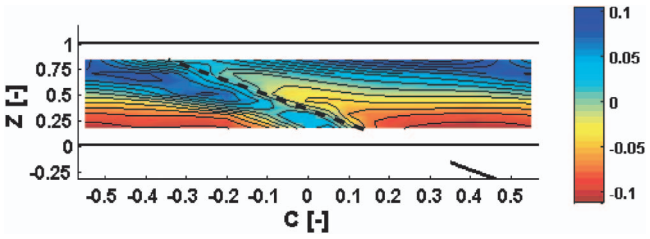

Fig. 5 Radial velocity v_r[−], R=1 (tip radius)

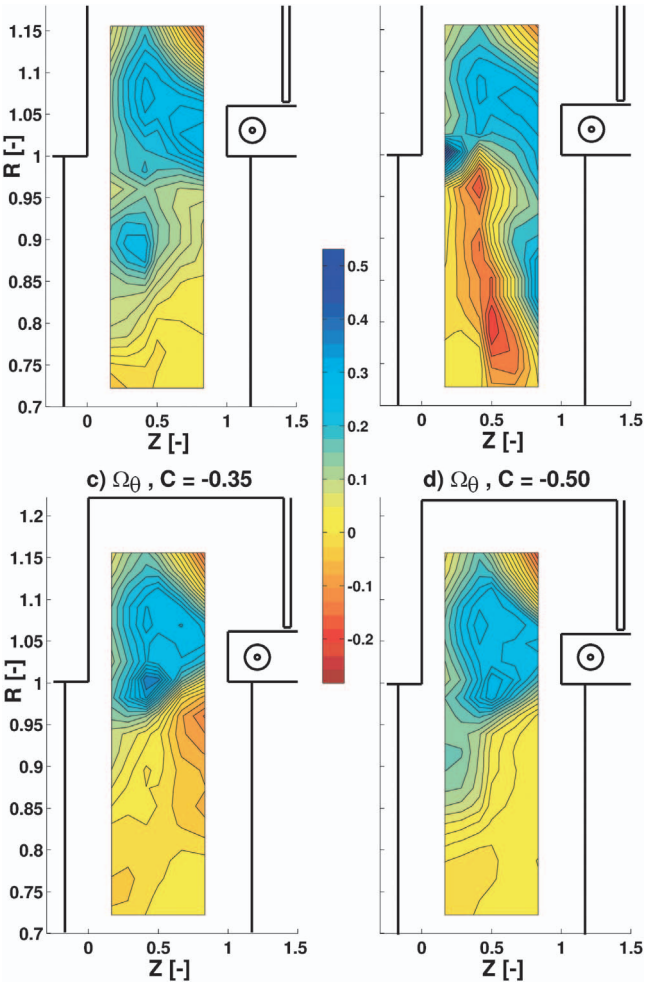

Fig. 7 Circumferential vorticity Ω_θ[−]

static pressure at $R=1.06$ coincides with streaks of higher total pressure. The inflow region marked with the arrow encounters a low local static pressure. High kinetic energy fluid is pushed into the cavity.

The convective path of flow in and out of the cavity is shown with a contour plot of radial velocity in Fig. 5. The view is in the positive radial direction. The thick line at $C=0.35$ indicates the position of the trailing edge at $R=1$. At $Z=0$ and 1 thick lines mark the axial position of the inlet corner and the shroud leading edge. Positive and negative radial velocities can be observed parallel to a line of zero radial velocity indicated with a dashed line. Close to the upstream corner radial velocities are negative, since the toroidal vortex pushes fluid into the main flow. On the downstream side of the axial gap the vortex moves fluid particles into the cavity. In addition, the centrifugal forces induced by the rotating shroud leading edge surface contribute to the inflow.

Vorticity Field. Flow in the cavity is three dimensional with a high level of unsteadiness in pressure and velocity. Representing the flow structure in terms of vorticity in this case permits a better physical insight into the entrainment and loss generation using only a single scaler. Figure 6 presents the non-dimensional circumferential and axial vorticity components of a circumferential position of $C=0.25$. The vorticity is made nondimensional assuming solid body rotation and taking a reference angular speed calculated with the blade passing frequency. High positive tangential vorticity dominates the measurement volume inside the cavity. Maximum values occur in a round region at $Z=0.4$ and $R=1.07$ as well as in the vicinity of the shroud leading edge. Close to the corner formed by the sealing fin and cavity floor the sign of vorticity changes. This may indicate the presence of a second counterrotating vortex with the center approximately at $Z=1$ and $R=1.15$ as the circular arrow indicates.

The axial vorticity component shows an alternating pattern of high positive, high negative and back to high positive values at the $Z=0.17$ as R increases. Since axial vorticity in cylindrical coordinates is defined as $\omega_z=1/r\partial r v_\theta/\partial r-1/r\partial v_r/\partial\theta$, it is a measure of tangential shear, if radial shear is comparably small. The region of high and low axial vorticity at $R=1$ and $R=0.96$ is confining the center of the tangential momentum wake, which was found in Fig. 3(*e*). The higher axial vorticity at $R=0.9$ as well as the lower at $R=0.96$ is induced by the overturning profile also found in Fig. 3(*e*) at $R=0.94$. As the gradients in tangential velocity decrease with Z, the axial vorticity also decreases. Note that some negative axial vorticity is induced from the rotating shroud leading edge.

A combined view of axial and tangential vorticity reveals the center of the toroidal vortex. The condition for the center of a toroidal vortex is zero vorticity in radial and axial direction, which is fulfilled in the local maximum of tangential vorticity at $R=1.073$ and $Z=0.41$. Closer to the shroud the tangential vorticity stays positive. However, the axial vorticity becomes negative. These two conditions can be explained with a skewed boundary layer induced by the tangential shear and the radial pumping effect of the rotating shroud and rotor leading edge. An important finding is, that the center of the toroidal vortex is found to be at a slightly higher span than it was determined with circumferential averaged data in Fig. 3(*b*). This indicates a pitch wise variation of the vortex center.

In Fig. 7, the tangential vorticity component at different circumferential positions is presented. Taking $C=0.25$ as a starting point, the diagrams Fig. 7(*a*) through *d* follow the convective direction of the toroidal vortex at $C=-0.05$, -0.35, and -0.5. In position $C=-0.05$ the main flow shows a high negative tangential vorticity. It is generated by the change of negative radial migration present in the blade wake with increasing Z. The high positive tangential vorticity at $R=1$ and $Z=0.17$ indicates the point on the pressure side of the stator wake where the inflow to the cavity starts. Comparing with Fig. 5, it seems that at $C=-0.35$, the region of high tangential vorticity is detached from the cavity corner and has moved into the midaxial gap position. This movement is continued in the next circumferential position while the magnitude of vorticity diminishes. At the end of the periodic cycle the region of higher vorticity merges with the flow region close to the shroud as can be observed in Fig. 6(*a*). It is through this process that vorticity is entrained into the toroidal vortex.

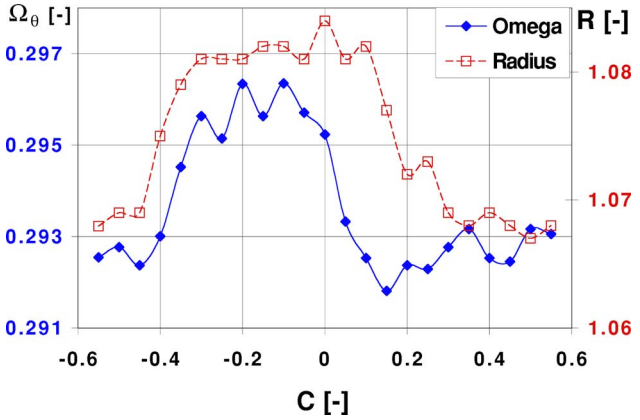

Fig. 8 Vorticity and radial position of the toroidal vortex

The radial position and the angular speed defined at the center of the toroidal vortex are presented in Fig. 8. As the cavity flow swirls in negative C direction, the vortex encounters stretching and tilting in the absolute frame. The cause of the spinning up and down of the vortex can be found in the static pressure field given in Fig. 4(*b*). Within the cavity at $C=0.4$ a local maximum of static pressure is observed, and vorticity of the toroidal vortex is low. The fluid within the vortex accelerates due to a favorable tangential static pressure gradient. At $C=-0.1$ the vortex reaches a low pressure field and vorticity is high. While passing one stator pitch the vortex is pushed outward to $R=1.08$ and the moves back to the lower radius $R=1.07$. The maximum absolute difference in radial position is 1.4 mm which is 7% of the cavity height. The resolution of the measurement grid in axial direction is not sufficient to detect an axial displacement of the vortex. Therefore, the axial position is given to $Z=0.41$ as discussed in Fig. 6.

Mass Flows Involved. The leakage mass flow, which passes the labyrinth, can be estimated using an empirical correlation. The correlation applied is given in Traupel [15],

$$\dot{m}_{\text{leak}} = Se\sqrt{p\rho} \tag{1}$$

where S is the gap area and e denotes the discharge coefficient. The latter depends on the pressure ratio and the number of sealing fins and was determined to be 0.17. With the conditions present in the inlet cavity to the labyrinth and the average gap width of 0.36% blade span the leakage mass flow is calculated to 0.52% of the main mass flow.

Table 2 compares the estimated leakage mass flow with the integrated probe measurements. The corresponding locations of integration are given in Fig. 9. Non-slip boundary conditions at $Z=0$ and $Z=1$ are considered in the integration procedure. The continuity of mass within the cavity states that all investigated mass flows must satisfy the equation

Table 2 Mass flows, % of main mass flow

Station	In ($v_r>0$)	Out ($v_r<0$)	Sum
1(a)	1.56	−1.44	0.12
1(b)	2.42	−1.85	0.57
2	⋯	−1.52	⋯
Traupel	⋯	⋯	0.52

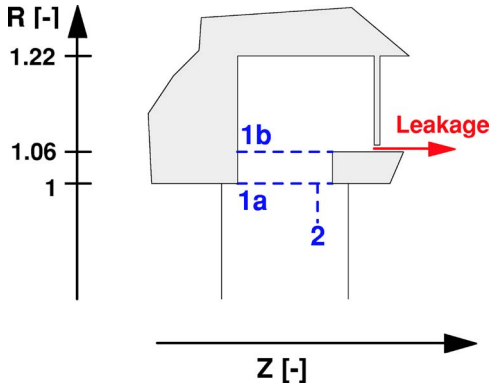

Fig. 9 Stations of mass flow integration

$$\dot{m}_{\text{leak}} = \dot{m}_{\text{in}} + \dot{m}_{\text{out}} \tag{2}$$

Integrating the radial velocity components at position 1a, gives a lower net mass flow than the estimated leakage mass flow. The grid spacing in axial direction is too coarse to capture the flow gradients close to the shroud leading edge. In addition, the toroidal vortex is cut far away from the center, which reduces the radial velocity components. At area 1b, much more rotating mass is involved, since this plane cuts the vortex close to the center. Furthermore, the new boundary layer at the shroud leading edge has grown, which results in an integrated mass flow close to the leakage mass flow.

In station 2 an area of $0.93<R<1$ and $-0.45<C<-0.1$ was integrated. This area fulfills two conditions. First, the streamlines have passed the outflow region on the suction side of the wake, e.g., in Fig. 5 $C=0.15\ldots0.2$ and $Z=0.25$. Second, the radial velocity is negative. The fluid particles enter the rotor passage. The axial velocity component sums up to 1.52% of the main mass flow, which is about three times higher than the leakage mass flow.

Integrating the tangential velocity components from $R=0.99$ to $R=1.22$ and $Z=0$ to $Z=1$, a swirling mass flow of 0.3% is found. The missing part of the cavity flow of $Z>1$ was estimated to have 0.1% assuming an average tangential velocity as in the measured part of the cavity flow. The swirling mass flow in the boundaries of $R=0$ to 0.99, and form trailing to leading edge was estimated at 1.7%. Therefore, the cavity flow comprises an estimated 24% of the swirling mass flow between the blade rows.

Relative Frame of Reference. In this section the measurement results of the virtual four sensor probe are presented in the relative frame of reference. Figure 10 shows the time averaged relative total pressure. The tip radius is indicated with a thick dashed line. The leading edge position of the rotor is given by the vertical dashed line at $C_{\text{rel}}=0$. The view is upstream and the arrow indicates the sense of rotation of the coordinate system.

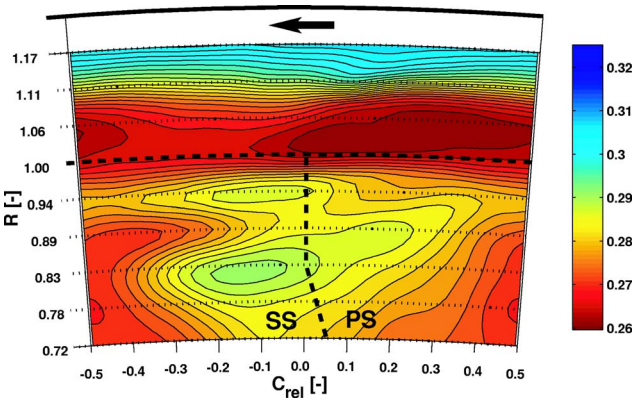

Fig. 10 Time averaged relative total pressure $C_{\text{porel}}[-]$ rotor relative, $Z=0.5$

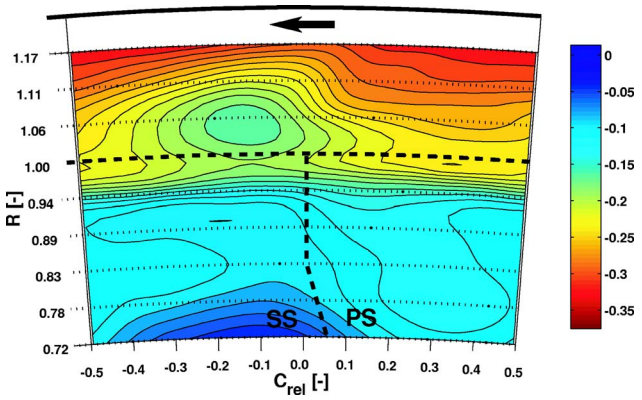

Fig. 11 Time averaged relative tangential velocity $v_{\theta\text{rel}}[-]$ rotor relative, $Z=0.5$

Within the cavity the relative total pressure shows a wavy structure but has a lower variation than in the main flow region. At the cavity floor, the relative total pressure is higher than upstream of the shroud leading edge.

The incoming flow field to the rotor passage is dominated by a high relative total pressure region at $C_{\text{rel}}=0$. The pressure contours are a result of two superimposed effects of the rotor blade on the upstream flow field. One is the leading edge potential field being responsible for an increase in static pressure. The other is found in the through flow distribution which is set up in a rotor passage due to the turning of the flow. The highest velocity is present on the suction side of an airfoil, where the local axial through flow reaches a maximum. The upstream effect of this interaction causes a higher relative dynamic head on the suction side of the leading edge. Figure 10 confirms this observation, where a region of higher relative total pressure at $C_{\text{rel}}=-0.15$ and $R=0.81$ is present.

The relative circumferential velocity distribution at $Z=0.5$ is given in Fig. 11. The cavity flow is swirling at a lower tangential velocity than the rotational speed of the rotor. Close to the cavity floor the values are high negative. The center of the cavity vortex at $R=1.07$ is accelerated and decelerated according to the static pressure field. The cavity vortex fluid moves into positive C_{rel} direction. The fluid is accelerated out of the high static pressure region across the leading edge position until it reaches the maximum relative velocity at $C_{\text{rel}}=0.4$. The static pressure there is therefore low. Close to the rotor leading edge the static pressure field induced by its potential field is clearly evident. Figure 12 shows a high static pressure upstream of the rotor leading edge. This pressure field propagates into the cavity at the speed of sound. In the main flow region a low pressure faces the rotor passage.

The potential field causes the distribution of relative radial velocity as presented in Fig. 13. In the time average the tip end wall of the rotor passage ($R=1$) exceeds positive and negative radial flow over the entire pitch. Additional radial inflow must occur closer to the shroud leading edge ($Z>0.83$) since the radial velocity is highly positive at $R=1.08$ and $C_{\text{rel}}=0.25$. Surprisingly, the highest positive radial velocity is not found at $C_{\text{rel}}=0$ directly above the leading edge. One reason could be that the relative movement of the fluid particles from the location of the inflow ($Z>0.83, C_{\text{rel}}=0$) up to the location of measurement results in a circumferential shift. Looking at the relative tangential velocity (Fig. 11), one can observe values of around –0.2 in the relevant area and an average radial velocity of 0.1 can be given. The di-

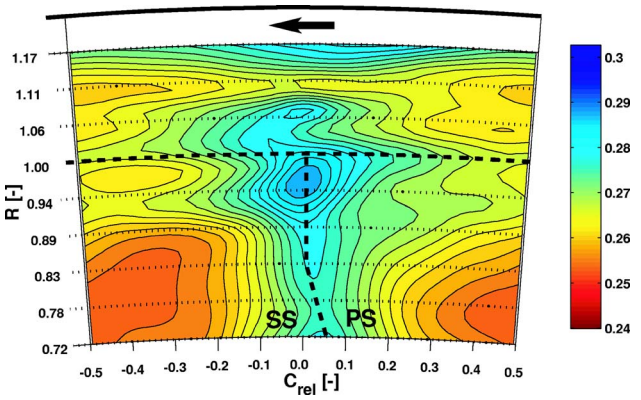

Fig. 12 Time averaged static pressure C_p[–] rotor relative, Z =0.83

rection of relative convection is indicated from the vector addition of the corresponding arrow of the radial and tangential velocity components. The resulting vector points from the intersection point of the stator leading edge and shroud to the maximum of radial velocity.

Unsteady Flow Field. The unsteady flow field is discussed with the help of Figs. 14 and 15, which show the non-dimensional total pressure and the non-dimensional tangential vorticity component. One period of rotor blade passing is resolved with four time frames. The data are given in the absolute frame of reference. The thick dashed lines indicate the blade tip radius as well as the leading edge position of the rotor. For clarity the latter is shown as a straight line.

The total pressure sequence starts with the rotor leading edge aligned with the stator wake. Comparing Figs. 4(a) and 14(a) the loss core has an increased value due to the potential effect. Following the time sequence the loss core region undergoes large changes in position, size and magnitude of pressure. If the open rotor passage is facing the loss core, as in t/T=0.5, the loss core covers a large area and values are low due to the accelerating lower static pressure.

Directing the attention to the cavity flow, regions of high and low total pressure are apparent. They move with rotor blade velocity. The high pressure region is ΔC=0.15 ahead of the rotor leading edge position. Note, that it is more round shaped and covers 30% of pitch, whereas the low pressure region is more narrow shaped and covers 70% of pitch. The low pressure region also coincides with the region of high negative relative tangential velocity in Fig. 11.

The wavy shear layer has changed the form in comparison to the time averaged picture. At C=0 in the initial time step the shear layer enters the main flow as deep as R=0.94. The S shape with the center at C=–0.1 is more pronounced. At t/T=0.25 it reaches to R=0.91 but has a minimum total pressure at R=0.96 and C =0. The outflow area, as it was determined in Fig. 4, undergoes unsteady periodic variations. The changes to the position of inflow (C=–0.25,R=0.98), however, are less affected by the rotor interactions.

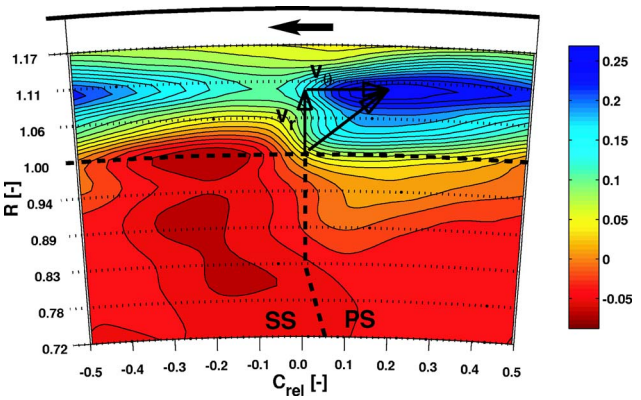

Fig. 13 Time averaged radial velocity v_r[–] rotor relative, Z =0.83

The rotor passage experiences an unsteady flow field as boundary condition. The mass flow is varying in time, since the area and velocity are changing with time. Recalling the results found of Table 2 in Fig. 9, unsteady fluctuations will also be encountered. Further investigations are planned to quantify the unsteady mass flow interactions with the rotor tip area.

The time sequence of the nondimensional circumferential vorticity component as given in Fig. 15 shows the unsteady vortex evolution within the cavity as well as the secondary flow field of the stator exit flow. At the first time step high positive values at C=0.1 and R=0.89 indicate the position of the passage vortex. The region of high negative values at C=–0.05 and R=0.8 coincides with the tangential total pressure gradient in Fig. 14. Radial migration within the wake and the loss core can have this effect on vorticity. The loss core region faces the rotor leading edge. As the rotor moves in time, both regions change their size and value. At t/T=0.5, the covered area is large and the measured vorticity values are lower than at the beginning of the sequence. Thus, the rotor passage is facing the loss core region.

The center of the toroidal vortex is found at radii around 1.1. This is located higher than the position determined with the five hole probe measurements in Fig. 8. Regions of high and low vorticity alternate in a similar manner as the total pressure in Fig. 14. The high vorticity coincides with low total pressure regions. Looking at the first time step t/T=0 the pitch wise variation of vorticity at R=1.1 ranges from 0.1 to 0.4. The maximum time averaged value found in Fig. 6 was 0.3. The vortex changes rotational speed in both space and time. The amplitude of the unsteady vorticity fluctuation is larger than the time averaged, pitch wise variations measured with the five hole probe in Fig. 8. The sign of vorticity does not change in time.

Furthermore, the unsteady mechanism of vorticity entrainment into the toroidal vortex can be discussed. The inflow region at R =1 and C=–0.35 encounters a local positive maximum of tangential vorticity [Figs. 4(a) and 8(b)]. While the region of high vorticity within the cavity passes this position, both areas merge together (t/T=0.74). Due to higher gradients vorticity is also transferred into the low vorticity regions of the toroidal vortex at this point (t/T=0.25).

Summary

Comprehensive Flow Model.

Overview. The flow field of the inlet cavity and the interaction zone is dominated by a three-dimensional, periodic unsteady static pressure field. Four independent sources of pressure fields are present:

- stator pressure field (uncovered turning);
- rotor pressure field (leading edge);
- cavity recess (step in and out); and
- annular casing (radial pressure gradient).

The periodic unsteadiness stems from the relative movement of the rotor pressure field. Due to the interference of the stator and rotor pressure field, the kinematic flow parameters, e.g., flow angles, velocity components, mass flows, experience high and low amplitudes, which depend on space and time.

The kinematic boundary condition to the flow area is set up by the stator exit flow containing wakes, boundary layers and secondary flow structures. This results in specific areas of inflow and

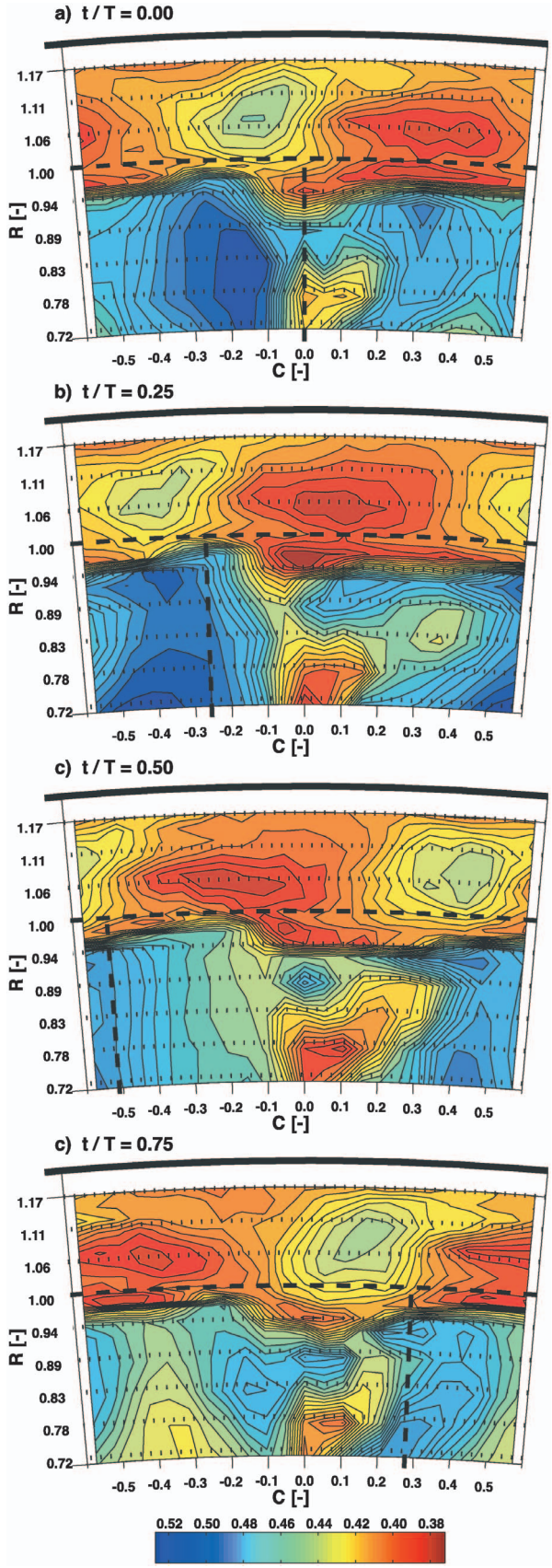

Fig. 14 Time sequence of total pressure C_{po}[−], Z=0.5

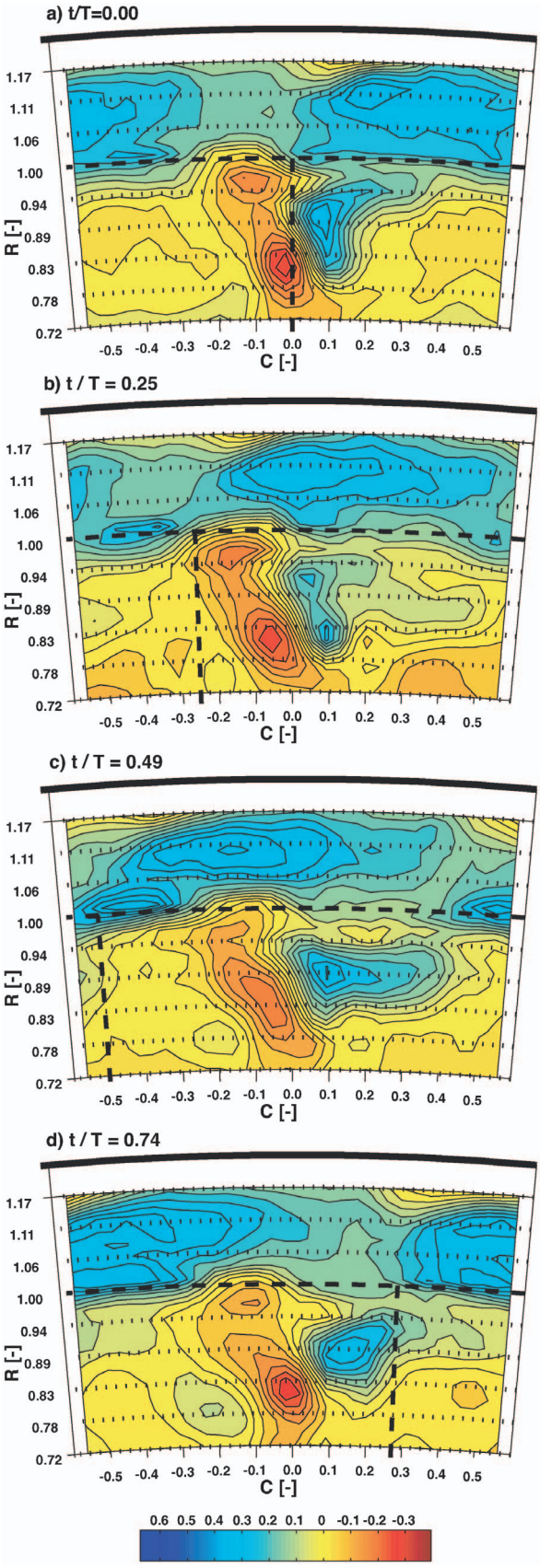

Fig. 15 Time sequence of tangential vorticity Ω_θ[−], Z=0.5

Table 3 Identified drivers of the toroidal vortex

	Stator	Rotor
Tangential momentum	In flow	Non-slip condition Potential field
Tangential vorticity	In flow Axial velocity shear profile	Radial pumping
Stretching	Potential field	Potential field

outflow for the cavity flow. Close to the exit of the flow area the kinematic effects are shaped by the radial pumping effect of the rotor leading edge alternating with the open rotor passage.

The interaction zone between main flow and cavity flow is dominated by a toroidal vortex. Additionally, this vortex moves at an average tangential velocity of 90% of the blade tip speed. This vortex undergoes stretching and tilting in space and time caused by different drivers of the cavity flow. They are summarized in Table 3.

Detailed Discussion. A sketch of the flow drivers is given in Fig. 16. The inflow and outflow regions are boundary conditions set by the exit flow field of the stator. The high potential fluid originating from the stator pressure side corner has enough kinetic energy to penetrate into the cavity. Radial equilibrium is not maintained in this area and the fluid follows a tangential direction, feeding tangential momentum to the cavity fluid. Due to the high axial velocity component, which is then turned into radial flow, the incoming fluid also contributes to the rotational movement of the vortex.

The outflow contains mixed cavity fluid of low total pressure, low tangential momentum, and negative incidence to the rotor tip profile section. This fluid affects the rotor passage flow field in an adverse way by increasing secondary flows and by doing less work on the rotor blades. Because of continuity, it balances the cavity inflow.

The cavity vortex system swirls at a lower velocity than the rotational speed of the shroud tip. This is due to mixing losses

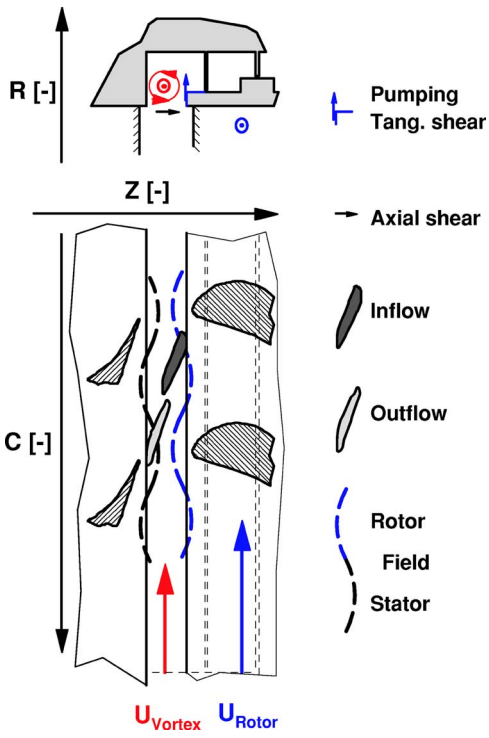

Fig. 16 Flow model: Side and above view

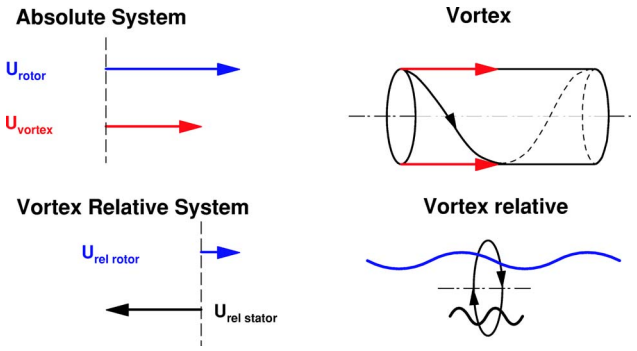

Fig. 17 Vortex relative system

within the vortices as well as to shearing effects of the boundary layer at the non-rotating walls. In addition the leakage mass flow transports tangential momentum into the next cavity.

In order to better understand the effects on the fluid movements, a flow relative system is helpful. A vortex relative coordinate system is proposed as described in Fig. 17. It rotates at the average tangential velocity of the toroidal vortex. By moving with the vortex in the swirling direction, rotor and stator events pass at two different relative velocities. These events correspond to two counter moving waves assuming rotor and stator pressure fields are standing sinusoidal waves in space. Then a dual frequency modulation acts on the vortex. Both frequencies satisfy the relation

$$f = f_{\text{rotor,rel}} + f_{\text{stator,rel}}. \tag{3}$$

In this case the frequencies are split into 17% of blade passing frequency for the rotor relative and 83% for the stator relative frequency. The wavelength of the two frequencies is also depicted schematically in Fig. 17.

Further investigations will be dedicated to derive a mathematical model by describing the flow in the vortex relative system. The goal is to model unsteady loss production terms and compare them to the experimental data in a quantitative way. A small perturbation analysis will then allow us to derive important parameters and scales for the loss production in this area. Additionally, the question might be answered as to whether unsteady loss is higher or lower than the steady loss. Future work will be dedicated to the mathematical modeling of the vortex and the quantification of steady and unsteady loss production terms with the help of the vortex relative system.

Impact on Efficiency. Using the available time averaged results, it is estimated that this labyrinth seal configuration results in a loss of about 1.6% per stage in efficiency for this turbine. The circumferential momentum of the leakage mass flow gets mixed out across the labyrinth. Measurements of the leakage jet entering the exit cavity indicate low circumferential momentum. The toroidal vortex by itself seems to contribute a small portion of efficiency loss around 0.1%. However, further losses in the rotor blade row due to the vortex interaction and the reentering cavity mass flow are not accounted for. These are estimated values based on the available data. It is planned that a more detailed integration and sensitivity analysis will be performed and presented at a later time. Additional measurements have been made with variations in seal clearance gap. Initial indications show that variation in the gap has a major effect on flow structures and turbine loss.

Conclusions

This paper presents a highly resolved experimental data set taken in an inlet cavity of a rotor tip labyrinth seal. The high resolution in space and time of flow angles and total and static pressure make it possible to derive further parameters, e.g., the velocity field or the vorticity field.

The drivers of the cavity flow could be identified. The unsteady flow interaction stems from the unsteady static pressure field interaction. The toroidal vortex found in the inlet cavity is described in detail. It is subject to unsteady vortex stretching and tilting. The total pressure fluctuations in the cavity outflow suggest an unsteady, low total pressure disturbance of the rotor tip region. Associated with this are a negative incidence and an average mass flow of 1.5% of the main mass flow. A vortex relative coordinate system swirling at the same average speed as the toroidal vortex is proposed.

Acknowledgment

The flow measurements in the turbine were supported by the German Federal Ministry of Economy (BMWI) under file Nos. 0327060D and 0327060F. The authors gratefully acknowledge AG Turbo, Alstom Power and Rolls-Royce Germany for their support and permission to publish this paper.

Nomenclature

a = speed of sound
r, θ, z = cylindrical coordinate system
h = blade height, 90 mm
z_{cav} = axial cavity width, 15 mm
n = numbers of blades, 42
f_{blade} = blade passing frequency
p = blade pitch, 360°/42
t = time
C = non-dimensional circumferential position θ/p
M = Mach number
R = non-dimensional radial height

$$\frac{r - r_{Hub}}{r_{Tip} - r_{Hub}}$$

Re = Reynolds number
T = blade passing period $1/f_{blade}$, temperature
U = blade tip speed
Z = non-dimensional axial distance z/z_{cav}
v = non-dimensional velocity u_{loc}/U
C_p = non-dimensional pressure

$$C_p = \frac{p_{local} - p_{stat,out}}{p_{total,in} - p_{stat,out}}$$

α = yaw angle
β = pitch angle
Ω = nondimensional vorticity $\omega/(4\pi f_{blade})$

References

[1] Gregory-Smith, D. G., Ingram, G., Jayaraman, P., Harvey, N. W., and Rose, M. G., 2001, "Non-Axisymmetric Turbine End Wall Profiling," Proc. Inst. Mech. Eng., **215**(A6), pp. 721–734.
[2] Sauer, H., Muller, R., and Vogeler, K., 2001, "Reduction of Secondary Flow Losses in Turbine Cascades by Leading Edge Modifications at the Endwall," J. Turbomach., **123**, pp. 207–213.
[3] Denton, J. D., and Johnson, C. G., 1976, "An Experimental Study of the Tip Leakage Flow around Shrounded Turbine Blades," CEGB research Report No. CEGB-R/M/N848.
[4] Peters, P., Breisig, V., Giboni, A., Lerner, C., and Pfost, H., 2000, "The Influence of the Clearance of Shrouded Rotor Blades on the Development of the Flow Field and Losses in the Subsequent Stator," ASME Paper No. GT2000-0478.
[5] Hunter, S. D., Manwaring, S. R., 2000, "Endwall Cavity Flow Effects on Gaspath Aerodynamics in an Axial Flow Turbine: Part 1-Experimental and Numerical Investigation," ASME Paper No. GT2000-065.
[6] Wallis, A. M., Denton, J. D., and Demargne, A. A. J., 2001, "The Control of Shroud Leakage Flows to Reduce Aerodynamic Losses in a Low Aspect Ratio, Shrouded Axial Flow Turbine," Appl. Math. Model., **123**, pp. 334–341.
[7] Anker, J. E., and Mayer, J. F., 2002, "Simulation of the Interaction of Labyrinth Seal Leakage Flow and Main Flow in an Axial Turbine," ASME Paper No. GT2002-30348, ASME Turbo Expo, June, Amsterdam.
[8] Schlienger, J., Pfau, A., Kalfas, A. I., and Abhari, R. S., 2003, "Effects of Labyrinth Seal Variation on Multistage Axial Turbine Flow," ASME Paper No. GT2003-38128.
[9] Pfau, A., Treiber, M., Sell, M., and Gyarmathy, G., 2001, "Flow Interaction from the Exit Cavity of an Axial Turbine Blade Row Labyrinth Seal," J. Turbomach., **123**, pp. 342–352.
[10] Binder, A., 1985, "Turbulence Production Due to Secondary Vortex Cutting in a Turbine Rotor," J. Eng. Gas Turbines Power, **107**(4), pp. 1039–1046.
[11] Chaluvadi, V. S. P., Kalfas, A. I., Baniegbal, M. R., Hodson, H. P., and Denton, J. D., 2001, "Blade Row Interaction in a High Pressure Turbine," AIAA J., **17**(4), pp. 892–901.
[12] Pfau, A., Schlienger, J., Kalfas, A. I., and Abhari, R. S., 2003, "Unsteady, 3-Dimensional Flow Measurement Using a Miniature Virtual 4 Sensor Fast Response Aerodynamic Probe (FRAP)," ASME Paper No. GT2003-38128.
[13] Sell, M., Schlienger, J., Pfau, A., Treiber, M., and Abhari, R. S., 2001, "The 2-Stage Axial Turbine Test Facility LISA," ASME Paper No. GT2001-0492.
[14] Treiber, M., Kupferschmied, P., and Gyarmathy, G., 1998, "Analysis of the Error Propagation Arising from Measurements with a Miniature Pneumatic 5-Hole Probe," *Proc., 13th Symp. on Measuring Techniques in Cascades and Turbomachines*, Limerick, Ireland.
[15] Traupel, W., 1977, *Thermische Strömungsmaschinen*, Springer, Berlin.